



HAL
open science

Facile membrane preparation from colloiddally stable metal-organic framework-polymer nanoparticles

Mingyuan Fang, J Cambedouzou, Didier Cot, Chaïmâa Gomri, Sabrina Nehache, Carmen Montoro, Mona Semsarilar

► **To cite this version:**

Mingyuan Fang, J Cambedouzou, Didier Cot, Chaïmâa Gomri, Sabrina Nehache, et al.. Facile membrane preparation from colloiddally stable metal-organic framework-polymer nanoparticles. *Journal of Membrane Science*, 2022, 657, pp.120669. 10.1016/j.memsci.2022.120669 . hal-03729759

HAL Id: hal-03729759

<https://hal.umontpellier.fr/hal-03729759v1>

Submitted on 20 Jul 2022

HAL is a multi-disciplinary open access archive for the deposit and dissemination of scientific research documents, whether they are published or not. The documents may come from teaching and research institutions in France or abroad, or from public or private research centers.

L'archive ouverte pluridisciplinaire **HAL**, est destinée au dépôt et à la diffusion de documents scientifiques de niveau recherche, publiés ou non, émanant des établissements d'enseignement et de recherche français ou étrangers, des laboratoires publics ou privés.

8 Facile membrane preparation from colloiddally stable Metal- 9 Organic Framework-polymer nanoparticles

10 Mingyuan Fang^a, Julien Cambedouzou^a, Didier Cot^a, Chaïmâa Gomri^a, Sabrina
11 Nehache^a, Carmen Montoro,^{*a,b} and Mona Semsarilar^{*a}

12 ^a Institut Européen des Membranes—IEM UMR 5635, Univ Montpellier, CNRS, ENSCM, 34095 Montpellier, France.

13 ^b Departamento de Química Inorgánica, Universidad Autónoma de Madrid, 28049 Madrid, Spain.

14
15 UiO-MOFs are based on zirconium cluster and carboxylic acid linkers. They have excellent
16 chemical and thermal stability, tolerance to linkers of different length and functionalities,
17 making them good candidates for a broad range of applications. However, difficulties of
18 processing the polycrystalline powder of MOFs limit their application. Here, we report for
19 the first time the synthesis of the UiO-66 in the presence of a well-defined poly
20 (methacrylic acid)-*b*-poly (methyl methacrylate) (PMAA-*b*-PMMA) nanoparticles (NPs)
21 prepared *via* Reversible Addition–Fragmentation Chain-transfer Polymerization
22 controlled Polymerization Induced Self-Assembly (RAFT-PISA). The PMAA-*b*-PMMA NPs
23 with multi carboxylic acid groups on their surface, well defined in shape and size, act as
24 multivalent connecting agent for the synthesis of the UiO-66. The resulting colloiddally
25 stable UiO-polymer NPs are crystalline, porous, and with an improved processability as
26 was demonstrated by the preparation of a thin film nanocomposite (TFN) membrane.
27 This membrane was applied in the filtration of Nickel(II) phthalocyanine-tetrasulfonic
28 acid tetrasodium salt aqueous solution obtaining a water permeability *circa* 20 L m⁻² h⁻¹
29 bar⁻¹ with a rejection of more than 90%. This unprecedented facile synthesis approach
30 could be universally applied to other MOFs, expanding their application in different fields
31 due to their enhanced processability.

32 1. Introduction

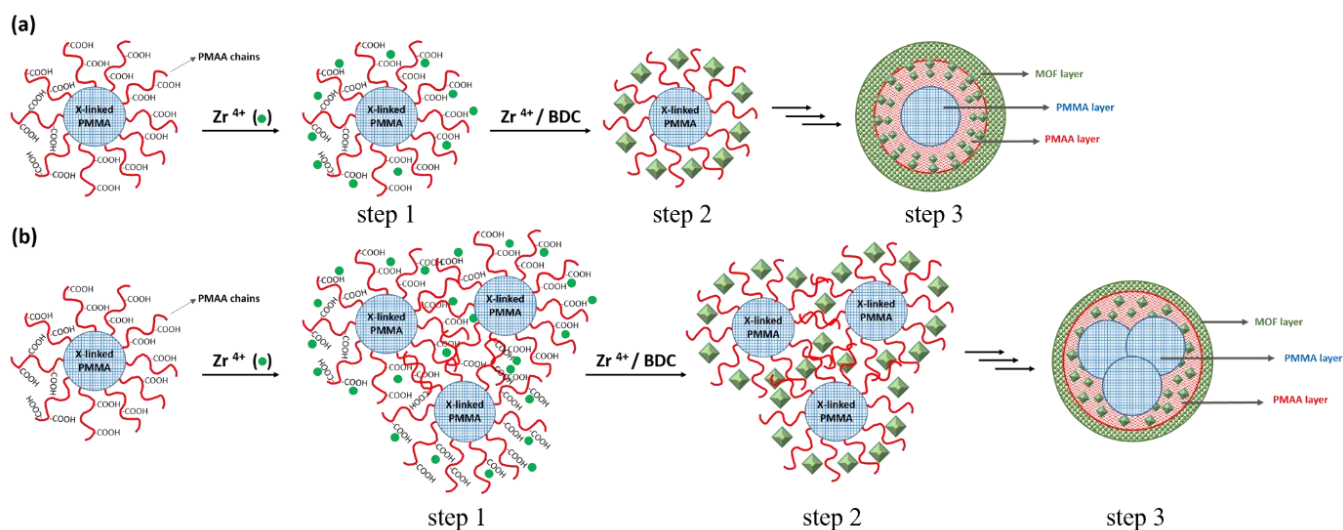
33 Metal Organic Frameworks (MOFs) are crystalline
34 and porous materials constructed from the
35 assembly of metal ions or clusters and organic
36 linkers through coordination bonds.[1],[2] They
37 show exceptional properties such as, high surface
38 areas, high thermal and chemical stabilities, they
39 make them useful in applications as varied as the
40 capture and separation of gases,[3],[4],[5]
41 catalysis,[6] drug delivery,[7] energy,[8],[9]
42 sensing[10] and water treatment.[11],[12]
43 Among numerous MOF structures reported, Zr
44 based MOFs have attracted considerable attention
45 in recent years due to their exceptional stability
46 different solvents, like water, acetone and *N,N*-
47 dimethylformamide (DMF).[13] In 2008, Lillerud
48 *et al.*[14] reported the first example of such structure,
49 UiO-66 (UiO from University of Oslo) based on Zr
50 cluster and a dicarboxylate linker. Later, UiO-66
51 series have been obtained by varying the
52 functionality as well as the length of the
53 dicarboxylate linker.[15],[16] However, the
54 crystalline nature of UiOs (and MOFs in general)
55 limit their application in many fields since shaping
56 and processing a polycrystalline powder is rather
57 complicated. Various studies have focused on

finding ways that facilitate MOF processing, mainly
in the form of membranes[17] or thin
films.[18],[19] One of the most used methods in
the preparation of MOF membranes, consists of
the dispersion of MOF within a polymeric matrix
resulting in formation of mixed matrix membranes
(MMMs).[20],[21] However, problems derived
from particle agglomeration, weak interactions
between MOF and the polymer matrix, results in
membranes with non-uniform particle distribution
and macro voids. To avoid particle-particle
interactions causing particle agglomeration,
Gascon *et al.*[22] recently demonstrated that
surface modification of large ZIF-67 nanoparticles
(NPs) using *N*-heterocyclic carbenes (NHCs), 1,3-
bis(2,4,6-trimethylphenyl)imidazole-2-ylidene
(IMes) and 1,3-bis(2,4,6-
diisopropylphenyl)imidazole-2-ylidene (IDip)
enhanced their processability in the liquid phase.
The outer surface functionalization of ZIF-67 gave
rise to MOF stable dispersions in non-polar
solvents which could easily be blended with two
polymer matrices (6FDA-DAM and 6FDA-DHTM-
Durene) and form mixed matrix membranes.
Alternative strategies are based on the surface

1 functionalization of MOFs NPs by polymers to tune
 2 both their inter-particle interaction and the
 3 interaction with the polymer matrix which gives
 4 rise to stable suspensions with improved
 5 processability.[23],[24] In this sense, the bottom
 6 up approach has also been employed to prepare
 7 colloidal dispersions of MOFs, where MOF
 8 synthesis is directly performed in the presence
 9 of polymers that act as soft templates or modulators.
 10 Lotsch *et al.*[25] used poly(acrylic acid) (PAA) and
 11 polyvinylpyrrolidone
 12 hexadecyltrimethylammonium bromide (PVP
 13 CTAB) to fine tune the particle size of HKUST-1 and
 14 IRMOF-3 within a large range (30–300 nm). Thin
 15 films were prepared via spin-coating using the
 16 MOF colloidal solution. In a different study PAA
 17 was used to synthesize UiO-66, resulting in narrow
 18 particle size distributions with high colloidal
 19 stability.[26]
 20 Apart from homopolymers, block copolymers have
 21 also been used in the synthesis of MOF structures
 22 (often as a soft template). Micelles formed from
 23 the self-assembly of amphiphilic block copolymers
 24 can act as surfactants, binding different

functionalities with the metal clusters, stabilizing
 the forming MOF structure in solution and avoiding
 the phase separation of the formed crystalline
 structures via coordinating micelles.[27]
 Polystyrene-*b*-(acrylic acid) and polystyrene-*b*-
 polyvinylpyridine were used as templates for the
 preparation of ZIF-8 and HKUST-1.[28] The
 oligomers were assembled in solution forming
 spherical micelles and acted as preferential sites
 for the nucleation of MOF templating the crystal
 growth. Mesoporous HKUST-1 was also prepared in
 presence of poly(MAA-*b*-EDMA).[29] Likewise,
 triblock copolymers such as poly(ethylene oxide)-*b*-
 poly(propylene oxide)-*b*-poly(ethylene oxide)s
 (PEO-*b*-PPO-*b*-PEO) has also been employed for
 the preparation of HKUST-1[30] and Ce-HMMOFs.[31]
 In this article, we report for the first time the
 synthesis of UiO-66 (Scheme 1) in the presence of
 well-defined core cross-linked poly (methacrylic
 acid)-*b*-poly (methyl methacrylate) (PMAA-*b*-
 PMMA) NPs prepared *via* Reversible
 Addition–Fragmentation Chain-transfer
 Polymerization (RAFT) controlled by
 Polymerization Induced Self-Assembly (PISA).

49 **Scheme 1.** Proposed mechanism for the synthesis of UiO-66 initiated from the surface of (a) one core
 50 cross-linked PMAA-*b*-PMMA spherical NPs, (b) an agglomeration of more than one PMAA-*b*-PMMA



51 spherical NPs connected through Zr^{4+} ions, serving as preferential anchoring site for the growth of UiO-
 52 66.

53
 54 These well-defined spherical NPs with multiple
 55 carboxylic acid groups on their surface, stable
 56 organic solvents, acted as nucleation sites for the
 57 synthesis of UiO-66. PISA has been developed for
 58 the facile synthesis of well-defined functional NPs
 59 with concentrations up to 50% w/w.[32] PISA
 60 formulations could be carried out in aqueous,[33]
 61 or organic solvents,[34] underlining the versatility
 62 of this approach. Here, an ethanolic PISA
 63 formulation was used to prepare the PMAA-*b*-

PMMA spherical NPs with high surface area. The
 shape, colloidal stability and the surface
 functionality of the NPs were well preserved in
 different solvents (ethanol, water and DMF, please
 see Fig. S1) thanks to their cross-linked core. The
 carboxylic acid functionalities provided a strong
 interaction sites for the Zr ions/clusters. In
 addition, the presence of the flexible PMAA
 chains expanding through the UiO crystallites could link
 different MOF phases, resulting in formation of a

1 homogeneous, stable colloidal solution. This could
2 simply be done by including the PMAA-*b*-PMMA
3 NPs in the classical formulation of UiO-66
4 synthesis. Processability of the synthesized UiO-
5 polymer NPs were tested *via* preparation of the
6 film nanocomposite (TFN) membrane by vacuum
7 assisted filtration of the UiO-polymer NPs on
8 nylon mechanical support. The prepared
9 membrane was used in the removal of Nickel(II)
10 phthalocyanine-tetrasulfonic acid tetrasodium salt
11 from water.

12 2. Materials and methods

13 2.1. Materials

14 Methacrylic acid (MAA) (4-methoxyphenol, MEHQ
15 used as inhibitor; 99.0%), 4-cyano-
16 (phenylcarbonothioylthio) pentanoic acid (>97.0%)
17 and 4,4'-azobis(4-cyanovaleric acid) (ACVA; 98.0%)
18 methyl methacrylate (MMA) (MEHQ used as
19 inhibitor, 99.0%), 2,2'-azobis(2-methylpropionitrile)
20 (AIBN; 98.0%), ethylene glycol dimethacrylate
21 (EGDMA) (MEHQ used as inhibitor; 98%)
22 (trimethylsilyl)diazomethane solution 2.0 M
23 diethyl ether, zirconium (IV) chloride ($ZrCl_4$; $\geq 99.5\%$
24 trace metals basis), acetic acid (glacial, $\geq 99\%$) and
25 nickel (II) phthalocyanine-tetrasulfonic acid
26 tetrasodium salt were purchased from Sigma
27 Aldrich and terephthalic acid ($\geq 98.0\%$), were
28 purchased from Alpha Aesar. Solvents were
29 purchased from Fisher Scientific and VWR. All the
30 reagents were used without further purification
31 Nylon membrane was purchased from Filtron
32 Fioroni, with an average pore size of 0.2 μm and
33 diameter of 47 mm.

34 2.2. Synthesis of poly(methacrylic acid) (PMAA)

36 PMAA macro chain transfer agent (mCTA) was
37 synthesized based on our previously published
38 work with some modifications.[35] MAA (12
39 135.3 mmol), 4-cyano-
40 (phenylcarbonothioylthio)pentanoic acid (540.8
41 mg, 1.93 mmol), and 4,4'-azobis (4-cyanovaleric
42 acid) (54.26 mg, 0.19 mmol; CTA/ACVA molar ratio
43 = 10) were dissolved in ethanol (12 g). The reaction
44 mixture was sealed in a vessel and purged with
45 nitrogen for 30 minutes and placed in a pre-heated
46 oil bath at 70 °C for 6 h. The polymerization was
47 quenched by cooling the reaction mixture to 20 °C
48 and subsequently exposing the mixture to the
49 The reaction mixture was diluted with a two-fold
50 excess of ethanol. The unreacted monomer was
51 removed by precipitation into a ten-fold excess

diethyl ether. The resulting solid was dried under
vacuum for 24 h. 1H NMR spectroscopy indicated a
mean degree of polymerization (DP) of 64 for the
PMAA macro-CTA, calculated by comparing the
integrated signals due to the aromatic protons at
7.2–8.0 ppm with those due to the MAA backbone
at 0.4–2.5 ppm.

2.3. Synthesis of poly(methacrylic acid)-*b*-poly(methyl methacrylate) diblock copolymer (PMAA-*b*-PMMA) NPs

61 (PMAA-*b*-PMMA) NPs were prepared *via* Reversible
62 Addition-Fragmentation Chain-transfer
63 Polymerization controlled Polymerization Induced
64 Self-Assembly (RAFT-PISA). A typical ethanolic RAFT
65 dispersion polymerization PMAA-*b*-PMMA
66 synthesis at 20 wt% solids was adapted from our
previously reported work. [35] MMA (0.9 g, 9
mmol), AIBN initiator (3.4 mg, 0.02 mmol), and
PMAA₆₄ macro-CTA (380 mg, 0.07 mmol) were
dissolved in ethanol (7 g). The reaction mixture was
sealed in a 10 mL round bottom flask and purged
with nitrogen for 10 min. The reaction flask was
kept in a preheated oil bath at 70 °C for 24 h. 1H
NMR analysis indicated that MMA about 95%
conversion was obtained after 26 h, a mean degree
of polymerization (DP) of 124 was calculated. The
PMAA-*b*-PMMA NPs were then cross-linked by
addition of 10% of EGDMA and the reaction was
carried out at 70°C for a further 12 h.

2.4. Synthesis of UiO-P-X% NPs

UiO-66 synthesis polymer-assisted was prepared by
using four different concentrations of the core
cross-linked PMAA-*b*-PMMA NPs in ethanol (10, 20,
40 and 80 % molar ratio of carboxylic acid function
of PMAA-*b*-PMMA to zirconium; see details in
Table S1). Briefly, $ZrCl_4$ (0.25 mmol, 58.3 mg) and
terephthalic acid (0.25 mmol, 40.3 mg) were
dissolved separately in 1.5 mL DMF. PMAA-*b*-
PMMA NPs were dispersed in 1 mL of DMF and
stirred for 1 hour. After that, this solution was
mixed with the $ZrCl_4$ solution and then the
terephthalic acid together with 0.5 mL of acetic
acid (30 equivalent) were added. The final mixture
was sonicated for 2 minutes and transferred to a
20 mL cylindrical glass pressure vessel that was
heated at 120 °C. After 20 hours, a light pink
colloidal or viscous solution of UiO-P-X% NPs in
DMF was obtained, where X represents the molar
percent of polymer NPs introduced into the
synthesis. So, the samples were denoted as UiO-P-
10%, -20%, -40% and -80%. To get the dry powder,
the light pink suspension was centrifuged at 4.4 K
rpm for 20 minutes and washed with 2 x 10 mL of

1 DMF and 3 x 10 mL of ethanol. Then, it was dried
2 under vacuum at 80 °C for 8 hours. 54
3 55
4 **2.5. Synthesis of UiO-66** 56
57
5 UiO-66 was synthesized using the method
6 previously reported by Behrens *et al.*[36] for 300
7 equivalent of acetic acid (see details in Table S10)
8 After 20 hours of reaction at 120°C, white powder
9 was obtained. The powder was centrifuged at 4.4k
10 rpm for 5 minutes, washed with 2 x 10 mL of DMF
11 and 3 x 10 mL of ethanol and finally dried under
12 vacuum at 80 °C for 8 hours. 66
13 67
14 **2.6. Kinetic study** 68
69
15 Synthesis of UiO-66 in presence of 20 mol%
16 PMAA-*b*-PMMA NPs (UiO-P-20%) was followed at
17 different intervals of time in order to establish the
18 possible formation mechanism. Samples were
19 taken at 0 min (T0min), 20 min (T20min), 40 min
20 (T40min), 1 hour (T1h), 2 hours (T2h) and 20 hours
21 (T20h). Thereafter, the evolution of particle size
22 and crystallinity of the samples were monitored by
23 SAXS and TEM analysis. 78
24 79
25 **2.7. Preparation of the membranes** 80
81
26 A TFN membrane was prepared by the 10 times
27 dilution of 0.1 mL of UiO-P-20% colloidal stable
28 solution in DMF and its deposition on a nylon
29 membrane substrate using a vacuum-assisted
30 filtration set-up. Then, the resulting TFN membrane
31 was washed with 2 x 5 mL DMF and 3 x 5 mL
32 ethanol. Finally, the membrane was dried under
33 vacuum at 80 °C for 8 hours. 89
34 The control membrane preparation was carried out
35 by depositing PMAA-*b*-PMMA solution on a nylon
36 substrate membrane (about 5 µL of PMAA-*b*-
37 PMMA ethanol solution diluted in 1 mL of DMF)
38 The supported membrane was washed with 2 x
39 mL DMF, 3 x 5 mL EtOH and dried under vacuum
40 80 °C for 8 hours. 96
41 97
42 **2.8. Characterization** 98
99
43 ¹H NMR spectra were recorded at room
44 temperature on a Bruker Advance spectrometer
45 400 MHz. Copolymer molecular weight
46 distributions were determined using size exclusion
47 chromatography (SEC) performed with a double
48 detector array from Viscotek (TDA 305, Malvern
49 Instruments, Worcestershire, UK). The Viscotek
50 apparatus was equipped with a two-column set-
51 up with a common particle size of 5 mm using
52 tetrahydrofuran (THF) as an eluent (1.0 mL min⁻¹)
53 The Viscotek system contains a refractive index
54 detector (RI, concentration detector). OmniSEC
55 software was used for data analysis and
56 acquisition. The number average molecular weights
57 (Mn) and the dispersity index (Đ) were calculated
58 relative to polystyrene standards. For SEC, the
59 polymers were modified by methylation of the
60 carboxylic acid groups on the PMAA block using an
61 excess of trimethylsilyldiazomethane. Briefly, 20
62 mg of the polymer or copolymer were dissolved in
63 THF and a yellow solution of
64 trimethylsilyldiazomethane was added dropwise at
65 room temperature. Upon addition, effervescence
66 was observed, and the solution immediately
67 became colorless. Addition of
68 trimethylsilyldiazomethane was continued until the
69 solution became yellow and effervescence ceased.
70 Then, a small amount of
71 trimethylsilyldiazomethane was added and the
72 solution was stirred overnight. The centrifuges
73 were performed through a Sigma Laboratory
74 centrifuge. X-ray diffraction (XRD) was performed
75 on a X'pert Pro (PAN Analytical). X-Ray
76 diffractometer in reflectance parallel beam/parallel
77 slit alignment geometry. The measurement
78 employed Cu Kα line focused radiation at 800 W
79 (40 kV, 20 mA) power. Samples were observed
80 using a 0.017° 2θ step scan from 5° to 50° with an
81 exposure time of 120 s per step. Small Angle X-ray
82 Scattering (SAXS) analysis were performed in the
83 transmission geometry of a laboratory set-up
84 available at the Institut de Chimie Séparative de
85 Marcoule. A GENIX Mo anode delivers an X-ray
86 beam of wavelength 0.711 Å after crossing a
87 XENOCs FOX2D monochromator. Collimation was
88 achieved using two sets of FORVIS scatterless slits.
89 Detection was made by a MAR345 imaging plate.
90 Capillaries of diameter 2mm were used as sample
91 holders. Absolute intensities were determined
92 after proper calibration using a Good fellow
93 polyethylene sample of width 2.36 mm and for
94 which absolute intensity was equal to 4.9 cm⁻¹ at
95 scattering vector q = 0.37 nm⁻¹. SAXS profiles were
96 simulated using the SASFit software.[37] Fourier-
97 transform infrared (FT-IR) spectra were performed
98 on a Thermo Nicolet iS50 FT-IR spectrometer in
99 transmission mode. Membrane FT-IR spectra were
100 performed on a Thermo Nicolet NEXUS FTIR
101 spectrometer with a diamond ATR attachment.
102 Thermogravimetric analysis (TGA) was measured
103 by TA Instruments SDT Q600 by heating the sample
104 to 1000 °C under nitrogen (100 mL min⁻¹) at a
105 heating rate of 10 °C min⁻¹. Nitrogen adsorption
106 isotherms were measured at 77 K on a
107 Micromeritics ASAP 2020 Plus Adsorption Analyzer.
108 Prior to measurement, powder samples were
109 degassed for 12 h at 373 K. Dynamic light scattering
110 (DLS) measurements were conducted on an Anton-

1 Paar Litesizer 500 at 20 °C. The DLS samples were
 2 diluted (50 folds) as compared to the original NP
 3 solutions. Scanning Electron Microscopy (SEM)
 4 images were observed under Hitachi S4800 with
 5 0.1–30 kV working voltage. Membrane cross
 6 sections for SEM analysis were prepared in liquid
 7 nitrogen via freeze-fracturing. Transmission
 8 Electron Microscopy (TEM) images were obtained
 9 from JEOL 1200 EXII (or JEOL 1400 Flash) and JEOL
 10 3000F under working voltages up to 120 kV and
 11 300 kV, respectively. TEM samples were prepared
 12 using 10 μ L of the sample placed on a carbon
 13 coated copper grid for 60 s. The PMAA-*b*-PMMA
 14 samples were stained using ammonium molybdate
 15 for 20 s. Then the grid was dried using a vacuum
 16 hose under ambient conditions. All the image
 17 analysis were performed using ImageJ software
 18 Optical microscope images were obtained by digital
 19 microscope Keyence VHX-7000.

20 2.9. Dye filtration experiment

22 The dye filtration experiment was carried out in
 23 filtration cell (Amicon 8010, 10 mL filtration cell)
 24 which was connected to a water reservoir and
 25 compressed air line. The effective area of the
 26 membrane based on UiO-P-20% was 4.9 cm² and
 27 the feed volume was 10 mL. The membrane was
 28 firstly stabilized *via* filtration of deionized water
 29 with gradual increasing pressure from 0.5 to 2 bar
 30 for 2 hours and then kept the pressure at 2 bar
 31 a further 2 hours. The excess of water was
 32 removed *via* dabbing with paper towel before
 33 performing the separation experiment. The
 34 experiment was performed at 0.5 bar using a
 35 aqueous solution of nickel (II) phthalocyanine
 36 tetrasulfonic acid tetrasodium salt (~0.04 mM)
 37 Between different cycles of experiments, dye
 38 solution was charged back to the filtration cell and
 39 the membrane was not washed in order to avoid
 40 the dilution of the dye solution. The volumetric flux
 41 (J_v , L h⁻¹ m⁻²) and the permeability (L_p , L h⁻¹ m⁻² bar⁻¹)
 42 of the membrane were calculated according to
 43 Darcy's law using the following equations:

$$J_v = \frac{V_p}{t \cdot S}$$

$$L_p = \frac{J_v}{\Delta P} \quad (2)$$

where V_p represents the permeate volume (L), t is
 the time for permeate collection (h), S is
 membrane nanofiltration area (m²) and ΔP is the
 pressure drop through the membrane (bar). The
 dye rejection was calculated by the equation:

$$D_{REJ} (\%) = [1 - \frac{C_p}{C_0}] \times 100 \quad (3)$$

where C_p and C_0 are the dye concentration in
 permeate and in feed solution, respectively. Both
 concentrations were determined by an UV
 spectrometer (SHIMADZU UV-2401PC
 spectrophotometer) at 625 nm that corresponds to
 the wavelength of maximum absorbance of nickel
 (II) phthalocyanine-tetrasulfonic acid tetrasodium
 salt.

60 3. Results and discussion

61 3.1. Characterization of the synthesized NPs

The spherical core cross-linked PMAA₆₄-*b*-PMMA₁₂₄
 NPs were synthesized in alcohol *via* RAFT mediated
 PISA, following our previously reported procedure.
 [35],[38] In brief, a well-defined PMAA macro-CTA
 with a mean DP of 64 ($M_n = 14.3$ kg mol⁻¹, $M_w =$
 14.9 kg mol⁻¹, $\bar{D} = 1.04$) was block extended with
 MMA in ethanol under dispersion PISA conditions.
 The resulting PMAA₆₄-*b*-PMMA₁₂₄ ($M_n = 18$ kg
 mol⁻¹, $\bar{D} = 1.19$) was core cross-linked *via* addition
 of EGDMA. The cross-linking of the core would
 prevent the NPs from solubilizing in organic
 solvents.

In order to have a larger surface area and more
 access to carboxylic functions on the surface of
 NPs, we chose to synthesize spherical PMAA-*b*-
 PMMA NPs (as compared to the other
 morphologies such as fibers and vesicles) that
 could provide more interactions with zirconium
 ions and Zr₆ clusters.

The morphology of PMAA-*b*-PMMA, UiO-P-X% NPs
 and UiO-66 MOF was analyzed by DLS, TEM and
 SEM (Table 1).

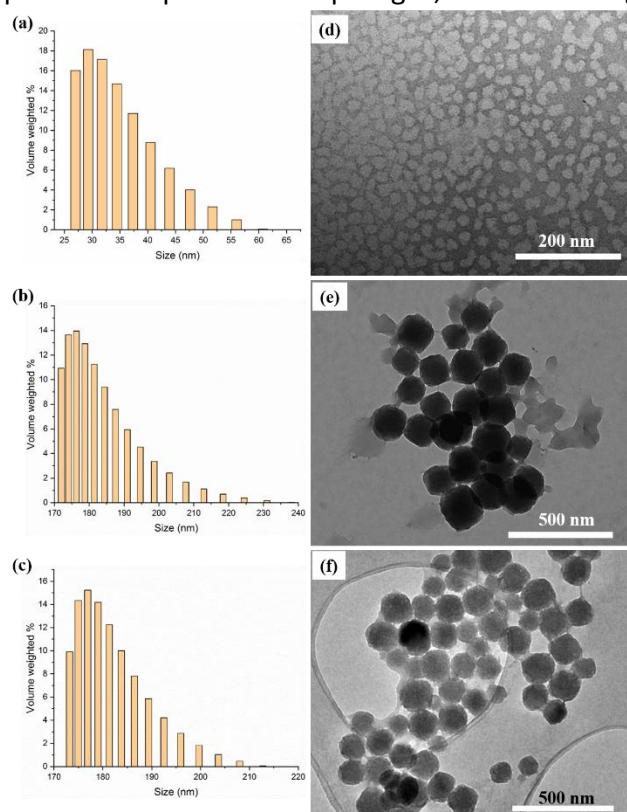
85 **Table 1.** NP size and particle morphology obtained using DLS, TEM and SEM.

Material	Size (nm) by DLS	Size (nm) by TEM	Size (nm) by SEM	Shape
PMAA- <i>b</i> -PMMA (Etanol)	37-44	23 ± 3	NA	Spherical
PMAA- <i>b</i> -PMMA (DMF)	27-56	34 ± 3	NA	Spherical
UiO-P-10%	170-240	144 ± 43	149 ± 24	Spherical

UiO-P-20%	170-220	130 ± 10	101 ± 18	Spherical
UiO-P-40%	175 - 265	65 - 210	70-200	Spherical
UiO-P-80%	128 - 228	50-110	57-160	Spherical
UiO-66	NA	500 ± 200	500 ± 200	octahedral

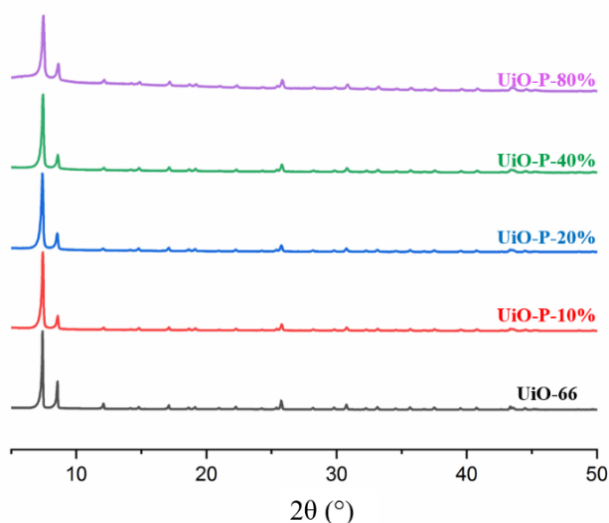
1
2 The hydrodynamic diameter of the PMAA-*b*-PMMA
3 NPs in ethanol was 40 ± 4 nm (Fig. S1a), and $34 \pm$
4 12 nm in DMF (Fig. 1a). The size of the spherical
5 NPs calculated using TEM images was 23 ± 3 nm
6 ethanol (Fig. S1b, S2a), and 34 ± 3 nm in DMF (Fig.
7 1d, S2b). The particles show similar hydrodynamic
8 diameter in ethanol and DMF by DLS and dry state
9 size (obtained from TEM image analysis). These
10 data indicate the preservation of the spherical
11 shape, size, and colloidal stability of the core cross-
12 linked PMAA-*b*-PMMA NPs in both solvents. The
13 size of the resulting UiO-P-X% NPs in DMF changed
14 according to the quantity of PMAA-*b*-PMMA NPs
15 introduced into the system.
16 When only 10% of polymer NPs was used,
17 crystallites with average size from 170 to 240 nm
18 were obtained (Fig. 1b). While when 20% of PMAA-*b*-
19 PMMA was introduced in the system, particle
20 size range was from 170 to 220 nm as judged
21 DLS measurements (Fig. 1c). When 40 mol %
22 polymer NPs were used, crystallites with size range
23 from 175 to 265 nm (175 - 224 nm mainly) were
24 obtained by DLS (Fig. S3a). While using 80 mol %
25 PMAA-*b*-PMMA NPs resulted in formation
26 particles with size of 128 - 228 nm (128-174 nm
27 mainly) (Fig. S3b). The NPs observed by TEM
28 showed a well-defined shape with a particle size of
29 144 ± 43 nm (Fig. 1e, S2c) for UiO-P-10% and $130 \pm$
30 10 nm (Fig. 1f, S2d) for UiO-P-20%. In case of UiO-
31 P-20%, no precipitation was observed after being
32 left unstirred for a month at ambient conditions
33 (Fig. S4). It seems that by increasing the quantity of
34 PMAA-*b*-PMMA NPs to 20 mol %, a good control
35 over the homogeneity and colloidal stability could
36 be reached. In contrast, when the amount of
37 PMAA-*b*-PMMA NPs were increased, the
38 crystallites of UiO-P-40% observed by TEM showed
39 a non-regular spherical shape with particle size of
40 65 to 210 nm (Fig. S3c) with 2 main populations
41 (100 to 160nm and 160 to 200 nm). It is more
42 difficult to observe individual crystallites in the
43 UiO-P-80% sample as the solution was very viscous
44 (gel-like) and difficult to re-disperse. The size of
45 these particles ranged between 50 to 110 nm. To
46 confirm that the stability of the hybrid particles
47 was due to the direct growth of the UiO-66
48 structure within the hairy shell formed by PMAA
49 chains, a mixture of pristine UiO-66 powders with
50 the 20 mol % of PMAA-*b*-PMMA NPs was prepared

in DMF (see supporting information for full details).
This mixture was colloiddally unstable and phase
separated rather rapidly after stopping the stirring
(Fig. S5). It could clearly be observed that the
growing of UiO-66 from the surface of the PMAA-*b*-
PMMA NPs totally changed the hydrodynamic
properties of the UiO-P-X% NPs as compared to the
core cross-linked polymer NPs. The shape of the
UiO-P-X% NPs were no longer perfectly spherical as
the edges started becoming angular and sharp (Fig.
1). UiO-P-X% powder isolated from the suspension
were also imaged using SEM and TEM and
compared to pristine UiO-66 (Fig. S6). Under SEM
the pristine UiO-66 showed polydisperse crystals
with octahedral shape with size range of 300 to
700 nm (Fig. S6a). Similar particles size could also
be observed under TEM with cubic shape showed
on two-dimensional TEM image (Fig. S6b). Shape
and size of the dry UiO-P-X% NPs were comparable
to what was observed for UiO-P-X% NPs in its
original state in DMF. UiO-P-10% and UiO-P-20%
crystallite size were 149 ± 24 nm and 101 ± 18 nm
respectively (Fig. S6c, S6d). UiO-P-40% presented a
spherical shape with sharp edges, with size range



1 of 70-200 nm (Fig. S7a, S7b). Shape and size of UiO-66
 2 P-X% crystallites could not be observed well under
 3 SEM, especially for the UiO-P-80%, since the MOR
 4 portion of the sample was rather little. Under SEM
 5 the UiO-P-80% (Fig. S7c, S7d) seems like

12 Structural characterization of UiO-P-X% was carried
 13 out by XRD measurements. The diffraction patterns
 14 (Fig. 2) show the major peaks of pristine UiO-66
 15 confirming the formation of the same crystalline
 16 structure. This means that the presence of PMAA-
 17 *b*-PMMA NPs does not affect the crystalline phase
 18 growth of the UiO-66. However, the intensity of
 19 the main signals decreased, and peaks became
 20 wider with the increasing amount of the
 21 amorphous polymer NPs.



22 **Fig. 2.** XRD patterns of pristine UiO-66, UiO-P-10%,
 23 UiO-P-20%, UiO-P-40% and UiO-P-80%.

24 The chemical composition of the hybrid UiO-P-X%
 25 NPs was analyzed by FT-IR measurements (Fig. 3).
 26 It was noted that the characteristic C=O stretching
 27 of the uncoordinated carboxylate group at 1730
 28 cm^{-1} and C-H stretching of methyl and methylene
 29 groups between 2995 and 2955 cm^{-1} from PMAA-
 30 PMMA NPs appeared in UiO-P-X% samples and the
 31 intensity of the bands increased with the increasing
 32 amount of the polymer NPs. The two intense bands
 33 around 1590 cm^{-1} and 1401 cm^{-1} are assigned to
 34 the asymmetric and symmetric stretch vibrations
 35 of C=O group, respectively, in the coordinated
 36 carboxylate group. Moreover, the band around 550
 37 cm^{-1} represents the Zr-(O=C) asymmetric stretch.
 38 [39], [40] These results indicate that PMAA-*b*-
 39 PMMA NPs are participating in the interaction with
 40 the metal clusters during the UiO-66 crystallites
 41 formation. The presence of PMAA-*b*-PMMA NPs in
 42 the synthesized materials was also corroborated by
 43 TGA (Fig. 4). The TGA profiles show that UiO-P-X%
 44 NPs go through a multistep gradual decomposition

continues polymer film with embedded UiO
 particles (size from 57 to 160 nm).

Fig. 1. Particle size distribution obtained from DLS
 for (a) PMAA-*b*-PMMA, (b) UiO-P-10% (c) UiO-P-
 20% in DMF and TEM images for (d) PMAA-*b*-
 PMMA, (e) UiO-P-10% and (f) UiO-P-20% in DMF.
 while pristine UiO-66 decomposed in three main
 steps. This difference is due to the presence of
 PMAA-*b*-PMMA NPs coordinated to UiO-66 NPs
 which decomposed in two steps. However, it is
 difficult to determinate the exact amount of
 incorporated PMAA-*b*-PMMA NPs since the organic
 linker decomposition of UiO-66 also takes place at
 the same temperature range (between 300 and
 500 °C). If the initial weight loss (due to free water
 loss below 100°C) is not accounted for, the weight
 loss of UiO-P-10% and UiO-P-20% at 800 °C is 5-7%
 higher than the pristine UiO-66. However, the
 additional weight loss at 800 °C for UiO-P-40% and
 UiO-P-80% were 17.6% and 24.7% higher than UiO-
 66 respectively.

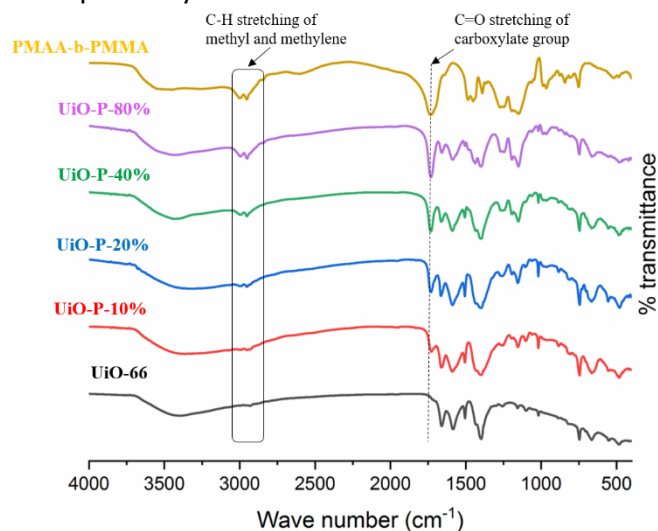
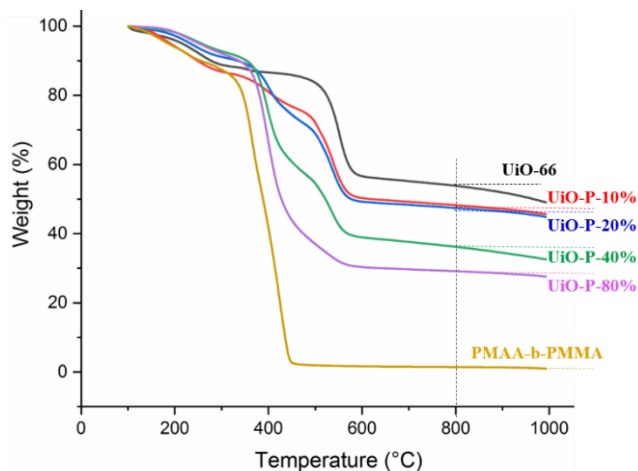


Fig. 3. FT-IR spectrum for UiO-66, UiO-P-10%, UiO-
 P-20%, UiO-P-40%, UiO-P-80% and PMAA-*b*-PMMA
 NPs.

The additional weight loss could also be an
 indication of the copolymer fraction incorporated
 in the hybrid structure (weight percentage of the
 PMAA-*b*-PMMA NPs present in the UiO-polymer
 hybrid structure). Moreover, it should be pointed
 out that incorporation of low amounts of polymer



1 NPs in the MOF structure (UiO-P-10% and UiO-P-20%) has a low impact on the thermal stability of the UiO-66.

2 20%) has a low impact on the thermal stability of the UiO-66.

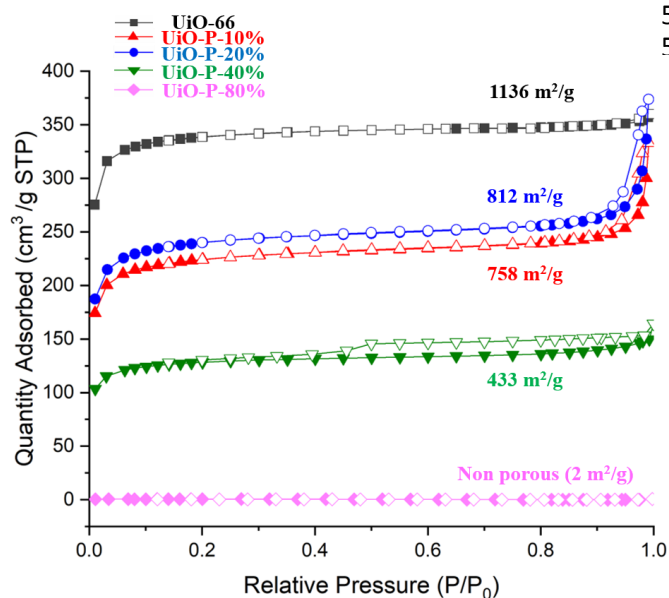
3 the UiO-66.

4 **Fig. 4.** TGA thermograms for pristine UiO-66, UiO-P-10%, UiO-P-20%, UiO-P-40%, UiO-P-80% and PMAA-*b*-PMMA NPs.

5 P-10%, UiO-P-20%, UiO-P-40%, UiO-P-80% and PMAA-*b*-PMMA NPs.

6 PMAA-*b*-PMMA NPs.

7 The nitrogen adsorption isotherms (Fig. 5) of pristine UiO-66, exhibit a typical type I isotherm at 77K with a Brunauer–Emmett–Teller (BET) surface area of 1136 m² g⁻¹ indicating the uniform microporous structure of UiO-66. UiO-P-10% and UiO-P-20% showed BET surface areas of 758 and 812 m² g⁻¹, respectively. As it was expected, the adsorption capacity decreased around 30 % with the decreasing size of the NP. This also highlights that the presence of the polymer NPs does not affect the accessibility of majority of the micropores in the MOF-polymer structure.



19 **Fig. 5.** N₂ adsorption isotherms measured at 77 K for pristine UiO-66, UiO-P-10%, UiO-P-20%, UiO-P-40% and UiO-P-80%. Filled and empty symbols represent adsorption and desorption, respectively.

20 for pristine UiO-66, UiO-P-10%, UiO-P-20%, UiO-P-40% and UiO-P-80%. Filled and empty symbols represent adsorption and desorption, respectively.

21 40% and UiO-P-80%. Filled and empty symbols represent adsorption and desorption, respectively.

22 represent adsorption and desorption, respectively.

23

24 However, the introduction of higher amounts of the non-porous polymer NPs has decreased the surface area, UiO-P-40% exhibit surface areas of 433 m² g⁻¹ (about 38% of surface area compared to pristine UiO-66). Then, when the PMAA-*b*-PMMA NPs content reach to 80 mol %, the obtained hybrid became nonporous with a BET surface area of only 2 m²/g. PMAA-*b*-PMMA NPs would become rigid and lose their flexibility under such low temperature. It is possible that the UiO-polymer hybrid could show better pore accessibility in solution. However, to confirm this a complete study needs to be carried out. The UiO-P-10%, UiO-P-20% and UiO-P-40% isotherms showed hysteresis

loops in the high relative pressure region, may indicate the appearance of mesopores by introducing the PMAA-*b*-PMMA NPs. The BJH desorption pore analysis (Fig. S10a and S10b) of UiO-P-10%, UiO-P-20% and UiO-P-40% showed small mesopores within the range between 3 and 4 nm. The UiO-P-10% and UiO-P-20% also presented large mesopores from 10 to 50 nm. One hypothesis about the source of large mesopores is that initial space occupied by the swollen polymer particles in DMF was partially released, because of the collapse of polymer particles during the drying and analysis under low temperature (Fig. S10c). More careful analysis is needed to investigate this effect. These results show that for having a performant MOF material the removal of the polymer particles is not necessary as the performance of resulting unprecedented UiO-polymer NPs are comparable to the pristine UiO-66 while showing immense improvement in terms of processability as it will be demonstrated below.

3.2. Kinetic study

2 With the aim to understand how the UiO-66 was formed in the presence of PMAA-*b*-PMMA NPs, a kinetic study was performed, monitoring the evolution of particle size and crystallinity by SAXS and TEM.

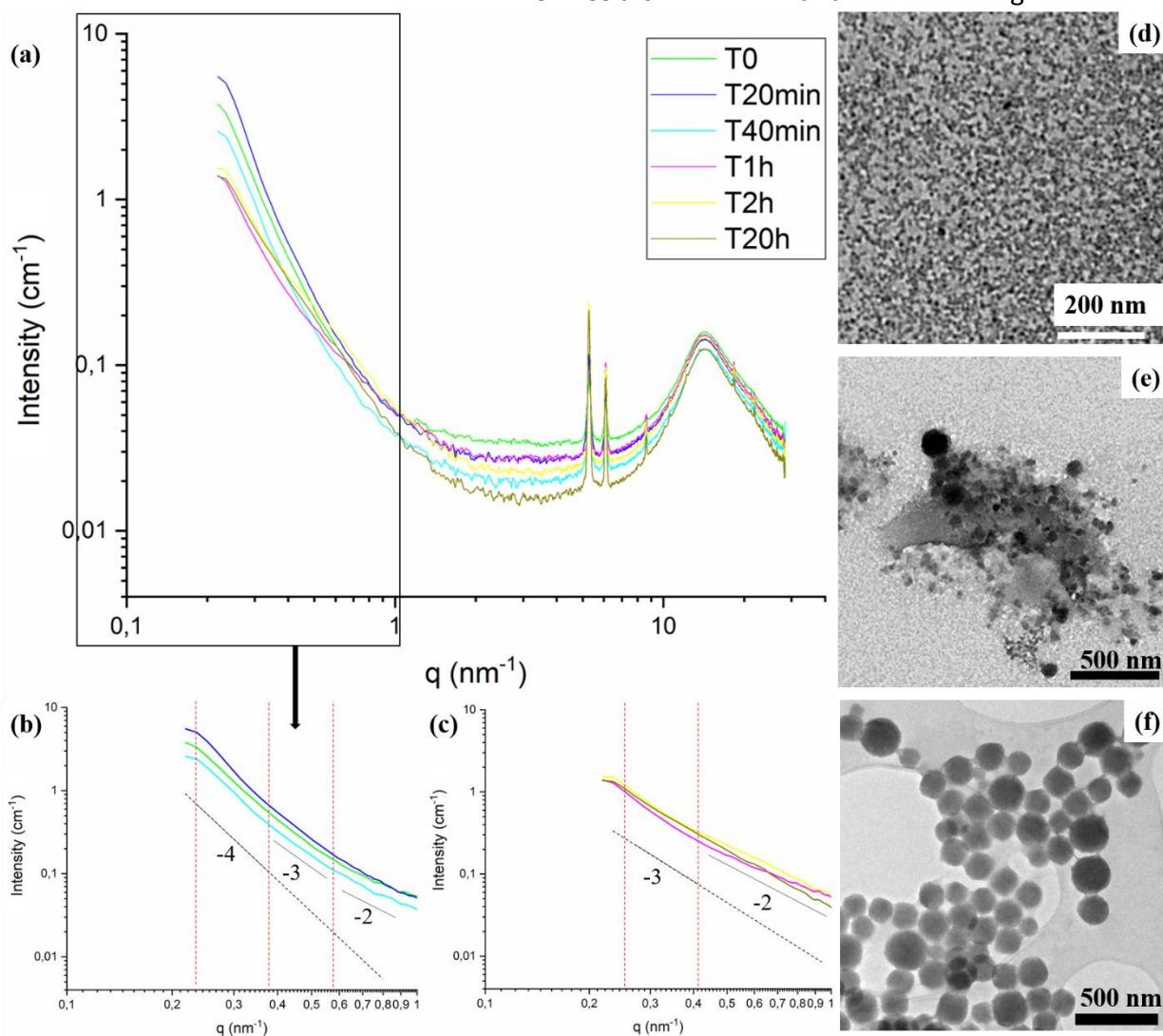
3 The SAXS profile of PMAA-*b*-PMMA NPs dispersed in DMF is shown in Fig. S8. At lower angles, the intensity decrease shows no specific feature until the appearance of two oscillations with intensity maxima located at scattering vector $q = 0.4$ and 0.6 nm^{-1} (Fig. S8a, S8b), respectively. Such oscillations could be related to the form factor of dispersed nanometric objects of size larger than 14 nm, whose lower angle signature involving the intensity plateau and the first oscillations are hidden by a more intense signal coming from other objects in the sample (e.g., particle substructure such as pores). Fig. S8c shows a simulation of the SAXS intensity originating from monodisperse spherical particles with diameter of 34 nm (obtained using the SASFit software). It can be seen that the two oscillations seen on the experimental pattern match the fourth and combination of fifth and sixth oscillations of the form factor of such objects, which are of similar size obtained from TEM and DLS.

4 Given the fast kinetics of the reaction, it was not possible to perform an in-situ SAXS experiment. Instead, samples at different time intervals were taken during the reaction. The SAXS pattern of the reaction mixture containing all the precursors for synthesis of UiO-P-20% (T0) shows two peaks at scattering vectors q of 5.27 and 6.10 nm^{-1} (Fig. 6a).

1 These two peaks correspond to the first two peaks
 2 of the typical UiO-66, indicating that there was
 3 already a small amount of UiO-polymer hybrid
 4 present in the reaction mixture. TEM analysis
 5 showed no large particles or crystals at this early
 6 stage (Fig. 6d). At 20 minutes, the reaction mixture
 7 started to turn opaque (as compared to
 8 transparent) and the two peaks at $q = 5.27$ and
 9 6.10 nm^{-1} became more intense. In addition, a new
 10 signal at $q = 8.61 \text{ nm}^{-1}$ appeared in the pattern (Fig.
 11 6a). These observations indicate the continuous
 12 growth of UiO-polymer hybrid crystals as a function
 13 of time. Similar trend could be observed in TEM
 14 images, where a large number of small crystals
 15 with size between 25 to 60 nm were visible (Fig.
 16 6e).

At 40 min, the reaction medium turned milky
 white. SAXS pattern showed more intense signals
 with two new peaks at $q = 10.55$ and 15.87 nm^{-1}
 that could highlight the enhancement of
 crystallinity and continuous growth of the UiO-66
 crystals on the block copolymer NPs. TEM images
 also showed the growth of UiO-P-X%. The size of
 the crystals was 80-120 nm with spherical
 morphology (Fig. S9a).

Similar trend could be observed for samples taken
 between 1 to 20 hours (T1h and T20h). SAXS
 patterns showed more and more intense peaks,
 referring to the enhancement of crystallinity (Fig.
 6a). TEM images revealed spheres with narrow
 distribution as a function of the reaction time (Fig.
 S9b-c and Fig. 6f).



33 **Fig. 6.** (a) SAXS pattern of UiO-P-20% T0min to T20h, (b-c) magnification of the SAXS patterns in the small
 34 angles region and the power laws of intensity in the region; TEM images for (d) T0, (e) T20min and (f)
 35 T20h.
 36

37 An important point to be noted in the SAXS
 38 patterns, is the slope of the linear regions between
 39 $q = 0.25$ to 0.4 nm^{-1} , 0.4 to 0.6 nm^{-1} and 0.6 - 1 nm^{-1} .
 40 These correspond to power laws in such log-log

1 representations of the SAXS patterns. They
2 changed significantly after 1 hour of reaction (Fig.
3 6b-c, Table S2). The power laws of the intensity
4 decrease before 1 hour (T0, T20min and T40m
5 samples) are respectively -4 from $q = 0.25$ to 0.56
6 nm^{-1} , -3 from $q = 0.4$ to 0.6 nm^{-1} , and -2 from q
7 0.6 to 1 nm^{-1} (Fig. 6b). Two inflexions could
8 found at $q = 0.4$ and 0.6 nm^{-1} , representing the
9 distances of $\sim 16 \text{ nm}$ and $\sim 10 \text{ nm}$. After 1 hour
10 reaction, the power laws of intensity in the region
11 where q ranges from 0.25 to 0.4 nm^{-1} decreased to
12 -3 (T1h, T2h and T20h). The change of power laws
13 in this region from -4 to -3 may indicate the
14 increasing of particle size of UiO-polymer hybrids.
15 This means that the -4-power law domain has been
16 shifted to the lower angles which is not reachable
17 with the used experiment set-up. Moreover, for
18 values ranging from 0.4 to 1 nm^{-1} , the power laws
19 decrease to -2 and the second inflexion point
20 lost (Fig. 6c).

21 The power law decrease at smaller angles (-4 to -3) may
22 correspond to the increase of the largest particles
23 roughness. In the q range between 0.4 and 0.6 nm^{-1} ,
24 is not easy to explain the change of intensity power law
25 from -3 to -2 in terms of morphological changes. The
26 evolution of the overall shape of the SAXS profile in the
27 mid- q range could also be attributed to an increase
28 intensity related to typical distances of 10-16 nm. Such
29 a signal could originate from the emergence of
30 porous organization at 10 nm scale, which also affects
31 the surface of NPs by increasing their roughness (Fig.
32 6f, S9d). The power laws in the range where q is larger
33 than 0.6 nm^{-1} are not relevant as intensity is low and
34 might be impacted by smaller intermolecular distances
35 in the sample.

36 3.3. Proposed formation mechanism and structure

37 Based on the previous results two formation routes
38 could be proposed (Scheme 1). The addition of the
39 acid decorated polymer NPs to the synthesis of
40 UiO-66 would result in the chelation of the
41 zirconium ions and clusters to the poly (methacrylate
42 acid) chains forming the shell of the polymer NPs
43 (step 1). From this point on the synthesis of the
44 UiO-66 would be carried out as in the case of
45 classical UiO-66 (steps 2 and 3). This route should
46 result in the formation of much smaller hybrid UiO-
47 polymer NPs as the initial size of the PMAA-
48 PMMA NPs were about 34 nm. The size of the
49 hybrid NPs calculated from the TEM images is
50 140 nm (4 times bigger than the polymer NPs). This
51 would mean that the UiO-66 would start growing

within the hairy PMAA chains, growing outwards,
until complete covering of the polymer NPs.
Complete coverage of the PMAA shell, should
result in the loss of colloidal stability of the hybrid
NPs, which is not the case here. The hybrid NPs
synthesized showed high colloidal stability over a
long period. This suggests that the second pathway
would be more probable. In the pathway depicted
in Scheme 1b, the preferential adsorption of the Zr
ions to the acid groups on the surface of the
particles would link two or more polymer NPs
together (step 1) where then the UiO-66 network
would start forming (step 2 and 3). The coagulation
of few polymer NPs would mean that less acid
groups would be engaged in the MOF formation
(hence more free acid groups). These results in
formation of a less dense layer of UiO-66, more
free acid groups penetrated through the thin layer
of UiO-66 that could explain the observed UiO-P-
X% particle size and their prolonged colloidal
stability.

3.4. Characterization of the membranes

Majority of MOF based-membranes are in the form
of MMMs. In such membranes, the MOF crystals
are dispersed in a polymer solution matrix prior to
casting. Although, extensively synthesized as used
specifically for gas separation, their weakness lies
in the fact that the two mixed materials (MOF and
polymer) are incompatible. This chemical
incompatibility results in inhomogeneous
distribution of the MOF fillers in the polymer
matrix. To date several different approaches have
been employed to homogeneously distribute the
MOF.[22],[25],[26]

The optimal properties of the UiO-P-20% NP
suspension in terms of particles size homogeneity
and colloidal stability, made it ideal for the
preparation of a TFN membrane which showed
good mechanical properties such as stability and
flexibility (Fig. 7a). The XRD (Fig. S11) and FT-IR (Fig.
S12) measurements showed that the crystallinity
and chemical functionalities of UiO-P-20% were
maintained during membrane preparation. The
TFN membrane was then observed under optical
microscope (Fig. 7b) to ensure the full coverage
and fissure free layer of UiO-P-20% on the nylon
support. In addition, the membranes analysis using
SEM revealed a continuous layer and
homogeneous MOF-polymer NP distribution on the
surface of the membrane (Fig. 7c).

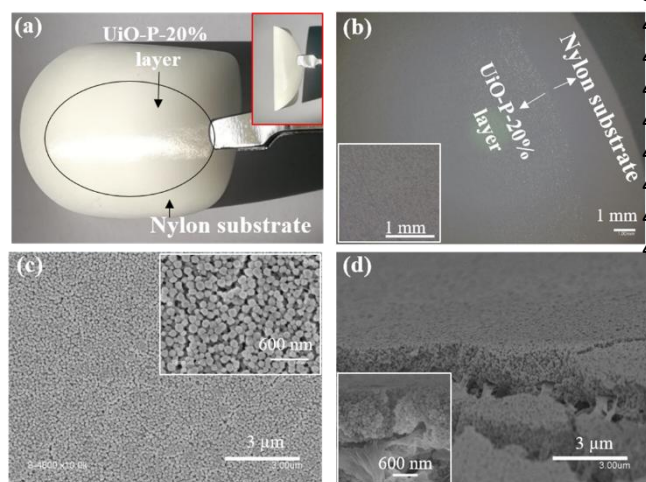


Fig. 7. UiO-P-20% nylon supported membrane images (a) optical, (b) optical microscope, and SEM (c) top view, (d) cross-section.

The cross-section SEM images of the membrane showed a compact thin film layer of UiO-P-20% NPs (Fig. 7d, Fig. S13) with an average thickness of 1 μm . For comparison, a control membrane was also prepared using a mixture of pristine UiO-66 powder and PMAA-*b*-PMMA NPs dispersed in DMF (Fig. S14). This membrane showed different aspects compared to UiO-P-20% nylon supported membrane. From the top view under SEM (Fig. S15 a-b), the membrane showed a non-continuous layer with numerous uncovered areas where the nylon support could be detected directly (inhomogeneous coverage with thickness from 0.8 to 3 μm).

3.5. Dye filtration experiment results

Membrane filtration properties were studied by the filtration of an aqueous solution of nickel (II) phthalocyanine-tetrasulfonic acid tetrasodium salt as guest molecule through the TFN membrane based on UiO-P-20%. The results showed that more than 90% of the dye was rejected (Fig. 8) from the solution compared to less than 9% of dye rejection by using the PMAA-*b*-PMMA membrane (Fig. S15) after 7 filtration cycles. In contrast, the average water permeability of the TFN membrane based on UiO-P-20% was around $20.4 \text{ L m}^{-2} \text{ h}^{-1} \text{ bar}^{-1}$ for the first 5 cycles (Fig. S16) which is largely less compared to $410 \text{ L m}^{-2} \text{ h}^{-1} \text{ bar}^{-1}$ of PMAA-*b*-PMMA membrane. This decrease in the permeability is clearly due to the presence of the UiO-66 structure with a different pore size as compared to those in the membrane prepared from block copolymer NPs. Through further image treatment, (distance map of binary images and manual measurement, see Fig. S17, S18; Table S3) and comparison

membrane permeability [35], an inter particle distance of approximately 12.4 nm could be estimated. The membranes were characterized after dye filtration using XRD (Fig. S11) and FT-IR (Fig. S12) to confirm the membrane stability. The results suggested that both crystallinity and integrity of the TFN membrane based on UiO-P-20% were perfectly maintained after the filtration process.

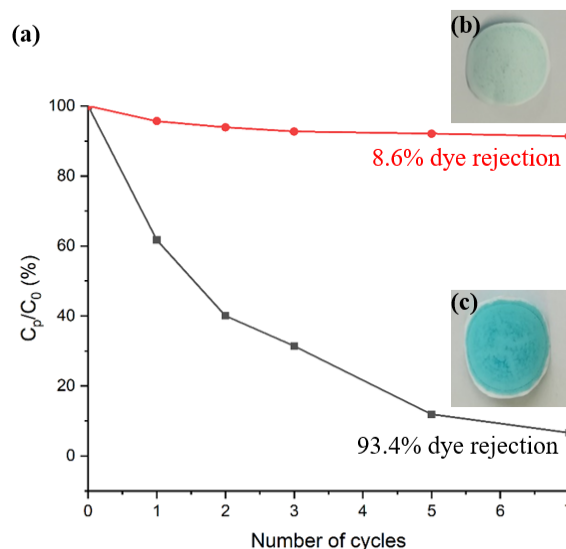


Fig. 8. (a) Dye concentration evaluation at different cycles, PMAA-*b*-PMMA membrane, UiO-P-20% membrane; Optical image of the nylon supported membranes after dye filtration (b) PMAA-*b*-PMMA (c) UiO-P-20% membranes.

4. Conclusions

A novel pathway for the synthesis of UiO-66 was carried out in the presence of well-defined spherical PMAA-*b*-PMMA NPs. Some of the resulting crystalline hybrid NPs were monodisperse and showed long-term colloidal stability. The core cross-linked spherical PMAA-*b*-PMMA NPs used in the presented approach is advantageous as a major challenge in the use of self-assembled surfactants and block copolymers in the synthesis of MOFs is the obligation to perform the synthesis in aqueous or alcohol media since the self-assembled structures would dissociate in organic solvents. However, majority of MOFs are synthesized in organic solvents such as DMF. The characterization of the resulting UiO-P-X% NPs both at colloidal and solid state indicated that they have comparable properties in terms of crystallinity, thermal stability, and porosity to the pristine UiO-66. This simple approach only requires the addition of the PMAA-*b*-PMMA NPs to the classical UiO-66 synthesis formulation and does not need any special treatment including the removal of PMAA-

1 *b*-PMMA NPs as often is the case when polymers
2 are used.[28] The incorporation of the diblock
3 copolymer NPs in the MOF structure renders high
4 colloidal stability and flexibility to the UiO-66
5 structure while maintaining the fundamental MOF
6 properties such as crystallinity and porosity.
7 Moreover, straightforward approach could be
8 easily applied for the synthesis of other carboxylic
9 acid-based MOFs with enhanced processability
10 unknown to MOFs, which would lead to their use in
11 numerous different applications since they could
12 be shaped and processed easily. To demonstrate
13 their processability a TFN membrane based on UiO-
14 P-20% NPs was prepared. Unlike other reported
15 membranes based on UiO or other families of
16 MOFs, the presented method here does not
17 require time-consuming mixing process with
18 polymer matrix nor chemical modification of the
19 matrix. The membrane properties and separation
20 capacity were verified using a model dye
21 compound. The results suggested that the UiO-
22 P-20% polymer selective layer, could reach rejection
23 values of more than 93%. This approach offers a
24 simple and highly adaptable pathway to make
25 robust membranes using different substrates
26 suitable for a wide range of application.

27 Author Contributions

28 The manuscript was written through contributions of
29 all authors. All authors have given approval to the final
30 version of the manuscript.

31 Conflicts of interest

32 There are no conflicts to declare.

33 Acknowledgements

34 Mathias Gravelle is thanked for his help with
35 experimental setups. MF acknowledges the
36 financial support of China Scholarship Council
37 (CSC), grant number 201708070001. INC-CNRS
38 thanked for the post-doctoral fellowship of CM. CM
39 also acknowledges the financial support of Madrid
40 Government under the Multiannual Agreement
41 with Universidad Autónoma de Madrid in the
42 context of the V PRICIT. (SI1/PJI/2019-00505)
43 Institut Carnot is also acknowledged for supporting
44 this project.

45 References

46 [1] H.-C. Zhou, J. R. Long, O. M. Yaghi, *Chem. Rev.* **2012**, *112*, 673.

- [2] N. Stock, S. Biswas, *Chem. Rev.* **2012**, *112*, 933.
- [3] L. J. Murray, M. Dinca, J. R. Long, *Chem. Soc. Rev.* **2009**, *38*, 1294.
- [4] E. Barea, C. Montoro, J. A. R. Navarro, *Chem. Soc. Rev.* **2014**, *43*, 5419.
- [5] V. Colombo, C. Montoro, A. Maspero, G. Palmisano, N. Masciocchi, S. Galli, E. Barea, J. A. R. Navarro, *J. Am. Chem. Soc.* **2012**, *134*, 12830.
- [6] A. Corma, H. Garcia, F. X. Llabres i Xamena, *Chem. Rev.* **2010**, *110*, 4606.
- [7] P. Horcajada, C. Serre, G. Maurin, N. A. Ramsahye, F. Balas, M. Vallet-Regí, M. Sebba, F. Taulelle, G. Férey, *J. Am. Chem. Soc.* **2008**, *130*, 6774.
- [8] P. Ramaswamy, N. E. Wong, G. K. H. Shimizu, *Chem. Soc. Rev.* **2014**, *43*, 5913.
- [9] C. Montoro, P. Ocón, F. Zamora, J. A. R. Navarro, *Chem. - A Eur. J.* **2016**, *22*, 1646.
- [10] L. E. Kreno, K. Leong, O. K. Farha, M. Allendorf, R. P. Van Duyne, J. T. Hupp, *Chem. Rev.* **2012**, *112*, 1105.
- [11] C. Wang, X. Liu, N. K. Demir, J. P. Chen, K. Li, *Chem. Soc. Rev.* **2016**, *45*, 5107.
- [12] M. S. Denny, J. C. Moreton, L. Benz, S. M. Cohen, *Nat. Rev. Mater.* **2016**, *1*, 16078.
- [13] Y. Bai, Y. Dou, L. H. Xie, W. Rutledge, J. R. Li, H. C. Zhou, *Chem. Soc. Rev.* **2016**, *45*, 2327.
- [14] J. H. Cavka, S. Jakobsen, U. Olsbye, N. Guillou, C. Lamberti, S. Bordiga, K. P. Lillerud, *J. Am. Chem. Soc.* **2008**, *130*, 13850.
- [15] S. J. Garibay, S. M. Cohen, *Chem. Commun.* **2010**, *46*, 7700.
- [16] J. Ru, X. Wang, F. Wang, X. Cui, X. Du, X. Lu, *Ecotoxicol. Environ. Saf.* **2021**, *208*, 111577.
- [17] X. Li, Y. Liu, J. Wang, J. Gascon, J. Li, B. Van Der Bruggen, *Chem. Soc. Rev.* **2017**, *46*, 7124.
- [18] Z. Liao, T. Xia, E. Yu, Y. Cui, *Crystals* **2018**, *8*, 338.
- [19] D. Zacher, O. Shekhah, C. Wöll, R. A. Fischer, *Chem. Soc. Rev.* **2009**, *38*, 1418.
- [20] L. Paseta, D. Antorán, J. Coronas, C. Téllez, *Ind. Eng. Chem. Res.* **2019**, *58*, 4222.
- [21] B. Seoane, J. Coronas, I. Gascon, M. E. Benavides, O. Karvan, J. Caro, F. Kapteijn, J. Gascon, *Chem. Soc. Rev.* **2015**, *44*, 2421.
- [22] A. Knebel, A. Bavykina, S. J. Datta, L. Sundermann, L. Garzon-Tovar, Y. Lebedev, S. Durini, R. Ahmad, S. M. Kozlov, G. Shterk, M. Karunakaran, I. D. Carja, D. Simic, I. Weilert, M. Klüppel, U. Giese, L. Cavallo, M. Rueping, M. Eddaoudi, J. Caro, J. Gascon, *Nat. Mater.* **2020**, *19*, 1346.
- [23] M. Kalaj, K. C. Bentz, S. Ayala, J. M. Palomba, K. S. Barcus, Y. Katayama, S. M. Cohen, *Chem. Rev.* **2020**, *120*, 8267.

1 [24] F. Jin, J. Liu, Y. Chen, Z. Zhang, *Angew.*
2 *Chemie - Int. Ed.* **2020**, 60, 14222.
3 [25] A. Ranft, S. B. Betzler, F. Haase, B. V. Lotsch,
4 *CrystEngComm* **2013**, 15, 9296.
5 [26] K. C. Bentz, S. Ayala, M. Kalaj, S. M. Cohen,
6 *Aust. J. Chem.* **2019**, 72, 848.
7 [27] M. L. Hu, M. Y. Masoomi, A. Morsali, *Coord.*
8 *Chem. Rev.* **2019**, 387, 415.
9 [28] S. Cao, G. Gody, W. Zhao, S. Perrier, X. Peng,
10 C. Ducati, D. Zhao, A. K. Cheetham, *Chem. Sci.*
11 **2013**, 4, 3573.
12 [29] H. Martínez-Pérez-Cejuela, M. Guiñez, E. F.
13 Simó-Alfonso, P. Amorós, J. El Haskouri, J. M.
14 Herrero-Martínez, *Microchim. Acta* **2020**, 187, 1.
15 [30] M. H. Pham, G. T. Vuong, F. G. Fontaine, T. O.
16 Do, *Cryst. Growth Des.* **2012**, 12, 1008.
17 [31] K. Li, J. Yang, R. Huang, S. Lin, J. Gu, *Angew.*
18 *Chemie* **2020**, 132, 14228.
19 [32] N. J. W. Penfold, J. Yeow, C. Boyer, S. P.
20 Armes, *ACS Macro Lett.* **2019**, 8, 1029.
21 [33] N. J. Warren, S. P. Armes, *J. Am. Chem. Soc.*
22 **2014**, 136, 10174.
23 [34] M. J. Derry, L. A. Fielding, S. P. Armes, *Prog.*
24 *Polym. Sci.* **2016**, 52, 1.
25 [35] L. Upadhyaya, M. Semsarilar, R. Fernández-
26 Pacheco, G. Martinez, R. Mallada, A. Deratani, D.
27 Quemener, *Polym. Chem.* **2016**, 7, 1899.
28 [36] A. Schaate, P. Roy, A. Godt, J. Lippke, F.
29 Waltz, M. Wiebcke, P. Behrens, *Chem. - A Eur. J.*
30 **2011**, 17, 6643
31 [37] I. Breßler, J. Kohlbrecher, A. F. Thünemann, *J.*
32 *Appl. Crystallogr.* **2015**, 48, 1587.
33 [38] L. Upadhyaya, M. Semsarilar, S. Nehache, D.
34 Cot, R. Fernández-Pacheco, G. Martinez, R.
35 Mallada, A. Deratani, D. Quemener,
36 *Macromolecules* **2016**, 49, 7908.
37 [39] L. Valenzano, B. Civalleri, S. Chavan, S.
38 Bordiga, M. H. Nilsen, S. Jakobsen, K. P. Lillerud, C.
39 Lamberti, *Chem. Mater.* **2011**, 23, 1700.
40 [40] S. Chavan, J. G. Vitillo, D. Gianolio, O.
41 Zavorotynska, B. Civalleri, S. Jakobsen, M. H. Nilsen,
42 L. Valenzano, C. Lamberti, K. P. Lillerud, S. Bordiga,
43 *Phys. Chem. Chem. Phys.* **2012**, 14, 1614.
44